Rechargeable Li-ion Battery Anode of Indium Oxide with Visible to Infra-red Transparency

M. Osiak[1], W. Khunsin[2], E. Armstrong[1], T. Kennedy[3,4], C. M. Sotomayor Torres[2,5,6], K. M. Ryan[3,4], and C. O'Dwyer[1,4,7]

[1] *Department of Chemistry, University College Cork, Cork, Ireland*
[2] *Catalan Institute of Nanotechnology, Campus UAB, Edifici CM3, Bellaterra, 08193 (Barcelona) Spain*
[3] *Department of Chemical and Environmental Sciences, University of Limerick, Limerick, Ireland*
[4] *Materials and Surface Science Institute, University of Limerick, Limerick, Ireland*
[5] *Catalan Institute for Research and Advanced Studies (ICREA), 08010 Barcelona, Spain*
[6] *Department of Physics, Universidad Autonoma de Barcelona, Campus UAB, 08193 Bellaterra, Spain*
[7] *Micro & Nanoelectronics Centre, Tyndall National Institute, Dyke Parade, Cork, Ireland*

Unique bimodal distributions of single crystal epitaxially grown In_2O_3 nanodots on silicon are shown to have excellent IR transparency greater than 87% at 4 μm without sacrificing transparency in the visible region. These broadband antireflective nanodot dispersions are grown using a two-step metal deposition and oxidation by molecular beam epitaxy, and backscattered diffraction confirms a dominant (111) surface orientation. We detail the growth of a bimodal size distribution that facilitates good surface coverage (80%) while allowing a significant reduction in In_2O_3 refractive index. The (111) surface orientation of the nanodots, when fully ripened, allows minimum lattice mismatch strain between the In_2O_3 and the Si surface. This helps to circumvent potential interfacial weakening caused by volume contraction due to electrochemical reduction to indium, or expansion during lithiation. Cycling under potentiodynamic conditions shows that the transparent anode of nanodots reversibly alloys lithium with good Coulombic efficiency, buffered by co-insertion into the silicon substrate. These properties could potentially lead to further development of similarly controlled dispersions of a range of other active materials to give transparent battery electrodes or materials capable of non-destructive *in-situ* spectroscopic characterization during charging and discharging.

Introduction

The marked increase in portable electronic device sales together with huge demand for flat screen high-definition televisions (HDTVs) are the main driving forces behind the need for batteries and continued research into various materials and forms for transparent conducting oxides (TCOs) and similar coatings (1). Among TCOs, materials such as indium oxide (IO), tin oxide (TO) or tin-doped indium oxide (ITO) (2–6) and emerging alternatives such as graphene and Cu or Ag NWs for example (6,7), have been a consistent focus of research interest where transparency in

a useful visible range is matched by sheet resistances below 10 Ω/□ (9) ITO is the TCO used most often and its applications vary from thin film transistors (10–12) to transparent contact in solar cells (5). Low sheet resistances are typically required for thin-film solar cells and the solar photon flux-weighted optical transparency of ITO on glass is about 80%. The battery however, a key component in the majority of portable electronics, has only very recently been demonstrated as a transparent device (13), and there is room for the development of true see-through charge storage materials (14–17). Their metallic properties cause most TCO's to be reflective in the infrared and for most TCO's a trade-off exists between transparency, conductivity, and sheet resistance for thin films (18). In line with this, transparency in battery electrodes gives the opportunity for *in-situ* and non-destructive diagnostic analysis of material changes during battery operation. This research could also allow the possibility of investigating kinetics of intercalation mechanisms and the influence of certain lithiated phases of TCO materials on transparency and conductivity.

Here, In_2O_3 {111}-oriented crystalline nanodot dispersions have been successfully grown from an MBE deposition of an In layer and subsequent oxidation at elevated temperature. The method results in unique areal and size dispersions of nanodots varying in size from hemispherical 2 nm dots to larger, faceted ~500 nm crystals, on the Si current collectors. Angle-resolved transmittance measurements confirm that the deposits maximize transparency in the infra-red, while maintaining characteristic transparency in the visible with a beneficial reduction in resistivity and sheet resistance; this overcomes the transparency limitations for In_2O_3 nanomaterials by index matching with air through a unique size dispersion. The nanodots form as $In@In_2O_3$ core-shell crystals, and form a stable solid electrolyte interface (SEI) layer and reversibly alloy with lithium allowing them to function as visible-to-IR transparent, visibly antireflective Li-ion battery electrodes. The approach shown here is straightforward and scalable and may be applied to the fabrication of high quality optoelectronic, electronic and sensor devices. Moreover, it could introduce visible-to-IR transparent conducting TCOs that reversibly store (electro) chemical charge, and also develop non-destructively, optically addressable materials and interfaces for *in-situ* monitoring of electrochemical processes.

Experimental

Before growth on silicon and glass substrates, the respective surfaces were cleaned using a standard RCA process. After rinsing, a second treatment in a H_2O_2:HCl:H_2O (1:1:5) solution was used to remove metallic and organic contamination. For evaporation of the In sources, a home-built MBE high-vacuum chamber with a distinct effusion cell for In together with an electron-beam evaporator was designed in cooperation with MBE-Komponenten GmbH As detailed Fig. 1, a uniform layer of In metal was deposited at a rate of 0.1 Å s^{-1} at a substrate temperature of 400°C, with precise control over the nominal thickness.

Surface morphologies and the chemical composition of the nanostructured dispersions were investigated by electron microscopy using a Hitachi SU-70 SEM with an Oxford-50mm^2 X-Max detector for energy dispersive X-ray analysis and Oxford Instruments Nordlys EBSD detector with HKL Channel 5 acquisition software. The size distribution of the nanodots was analysed using ImageJ (19).

X-ray photoelectron spectroscopy was acquired using a Kratos Axis 165 monochromatized X-ray photoelectron spectrometer equipped with a dual anode (Mg/Al) source. Survey spectra were captured at as pass energy of 100 eV, step size of 1 eV, and dwell time of 50 ms. The core level spectra were an average of 10 scans

captured at a PE of 25 eV, step size of 0.05 eV, and dwell time of 100 ms. The spectra were corrected for charge shift to the C 1s line at a binding energy of 284.9 eV. A Shirley background correction was employed, and the peaks were fitted to Voigt profiles.

Variable angle spectroscopic ellipsometry (VASE) was performed using a J. A. Woollam Co., Inc. M-2000U variable angle spectroscopic ellipsometer over a wavelength range of 300 to 900 nm. Reflectance measurements were carried out in a Bruker FT-IR spectrometer IFS66/V on nanodot samples and ITO on glass. Different configurations of beam splitters, detectors and sources were used to cover the infrared (5 μm) to visible ranges. For angular resolved measurements, a NIR512 Ocean Optics spectrometer was used as a detector in a home-built reflectance/transmittance setup using a collimated Xenon arc lamp as a light source.

To investigate the electrochemical insertion (alloying) and removal of Li, cyclic voltammetry measurements were carried out in a 3-electrode setup using a Multi Autolab 101 potentiostat, using Li as both counter and reference electrodes. All potentials, unless otherwise stated, are relative to Li^+/Li. Custom build swagelock-type cells were used with counter and active material electrode separated by a polypropylene separator soaked in 1 mol dm^{-3} solution of $LiPF_6$ in EC:DMC at a 50:50 v/v ratio. The electrode was cycled at a scan rate of 0.5 mV/s. Afterwards, the electrode was carefully washed in acetonitrile and a 10^{-4} mol dm^{-3} solution of acetic acid to remove the electrolyte residue.

Results and Discussion

Epitaxial growth of In_2O_3 nanodots

MBE deposition of indium and subsequent oxidation in ambient air allows the formation of a specific size dispersion of oxide crystals after In growth, as shown in Fig. 1a. The dispersion consists of larger crystals interspersed with a high density of very small (~2-5 nm) nanodots (Fig. 1b). Some of the larger crystals have clearly developed facets generally growing in a deviated hexagonal shape (Fig. 1b). High resolution SEM images of the nanodots show that a number of small crystallites are found on the top surfaces of the large crystals (Fig. 1b).

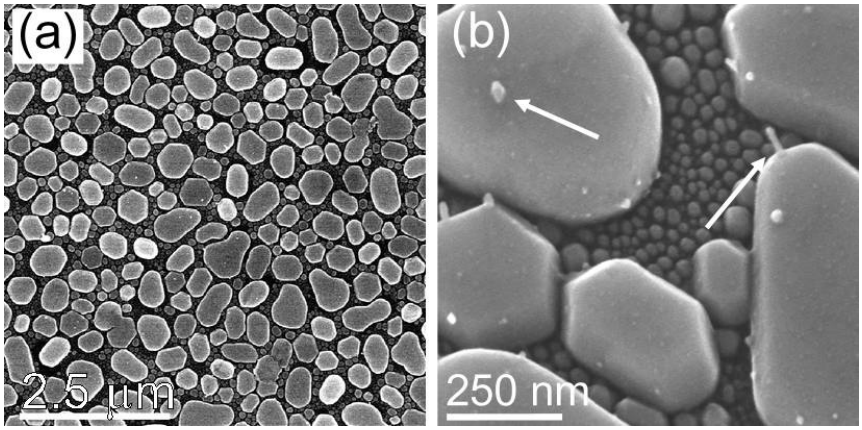

Figure 1. (a) SEM image showing the final epitaxial In_2O_3 nanodot dispersion on Si. (b) Tilted SEM image showing small, hemispherical nanodots interspersed between larger crystals. Arrows indicate small crystallites growing hierarchically on the top surfaces and nanowires growing from the edges of crystals.

The initial formation of a dewetted liquid In 'layer' comprising a high density of metallic nanodots (maintained in a liquid state on a substrate heated to 400 °C), and the progressive nature of their deposition allows hierarchical nanodot seeds to form on the high energy facet edges of the larger crystals. In some cases we observe subsequent growth of long, straight In_2O_3 nanowires (see Fig. 1b) with lengths reaching hundreds of nanometres and diameters not exceeding the diameter of hierarchical dots.

Electron backscattered diffraction from the terminating surfaces of both faceted and non-faceted nanodots was used to quantify their epitaxial relationship to their substrate and also their relative orientational distribution. The measurements were taken at 70° tilt (Fig. 2a) and a pole plot of the nanodot texture orientation distribution (Fig. 2b) was formed by monitoring the Kikuchi diffraction patterns from the top surface lattice planes of the nanodots shown in Figs 2c and d; the growth orientations from 3D crystal symmetry are visible as diffraction 'paths' in orientation-space. The measurements confirm a dominant {111} surface termination for the nanodots. Interestingly, for both faceted and non-faceted crystals, their terminating planes are near-identical, as are their overall heights of ~50 nm, see Fig. 2a.

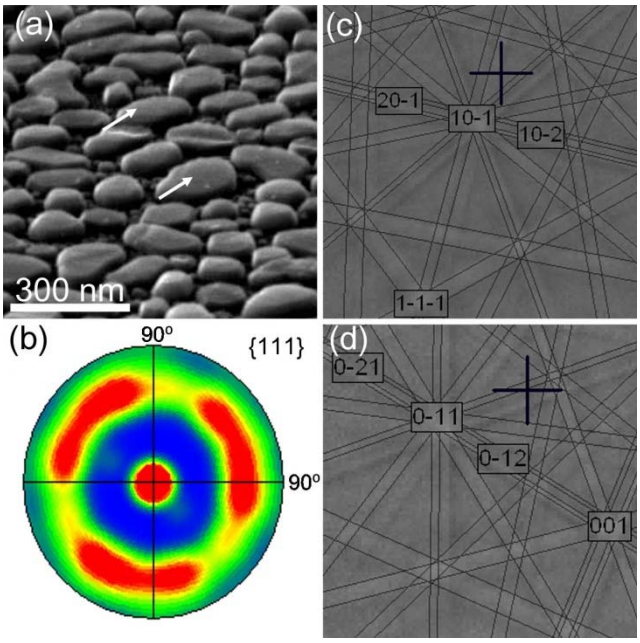

Figure 2. (a) SEM image of the In_2O_3 nanodots. Arrows indicate the location of the points at which the EBSD pattern was recorded. (b) Pole figure showing the relative orientation distribution of {111} termination of the nanodots. (c-d) Kikuchi band overlays recorded from the regions indicated in (a). The cross on each image indicates the orientation of the planes at their measurement point.

Being extremely sensitive to tilt or variations in the top surface of the crystals, the corresponding pole plot shown in Fig. 2b were acquired to map the distribution of textures around major growth directions. The texture pole plot is centered around the {111} directions. It is clear from the texture distributions in the in Fig. 2b, that the particles grow with horizontal hexagonal {111} planes, parallel to the (100) substrate of the silicon wafer. The In_2O_3 nanodots were epitaxially deposited as metal nanodot seeds and subsequently oxidized in air and EBSD analysis confirms that their oxidation to In_2O_3 nanodots results in a final single crystal structure with the {111} growth planes parallel to the substrate. The growth rate perpendicular to {111} places is comparatively slower than {110} and {100} planes. As a result, growth in lateral direction progresses faster than in the vertical, which we find regardless of the degree

of crystal faceting. Additionally, lattice mismatch ($f = (a_f - 2a_{sub})/2a_{sub}$ where a_f and a_{sub} are the lattice constants in the growth plane of In_2O_3(111) and Si(100), respectively) of In_2O_3 on silicon is only 1.13% resulting in low strain at the nanodot-substrate interface (20). This allows for minimizing of any additional strain placed on the deposit due to the electrochemical reduction from In_2O_3 to metallic In and subsequent volumetric expansion accompanying electrochemical Li insertion.

The composition of the MBE nanodots was determined using XPS and EDX. Figure 3a shows the In3d and O1s core-level photoelectron emission spectra of the nanodots. Core-level emission corresponding to In $3d_{5/2}$ and In $3d_{3/2}$ were observed at 444.34 eV and 452.03 eV (referenced to the C1s core-level of 284.9 eV) indicative of In_2O_3. The peak at 444.34 eV shows hyperfine levels, one at 443.9 eV from In(0) and at 445.1 eV related to In $3d_{5/2}$ from In_2O_3. Core-level emission from O 1s was composed of two spectral bands at 531.2 eV and 529.6 eV, which can be deconvoluted into three components consistent with In_2O_3. The signal at 531.2 eV is attributed to lattice oxygen, while that at 529.6 eV stems from some $In(OH)_3$, which is known to form from exposure of In_2O_3 to water vapour. Corresponding EDX maps of In and O (shown in Figs 3b-e) corroborate oxide composition of the nanodots.

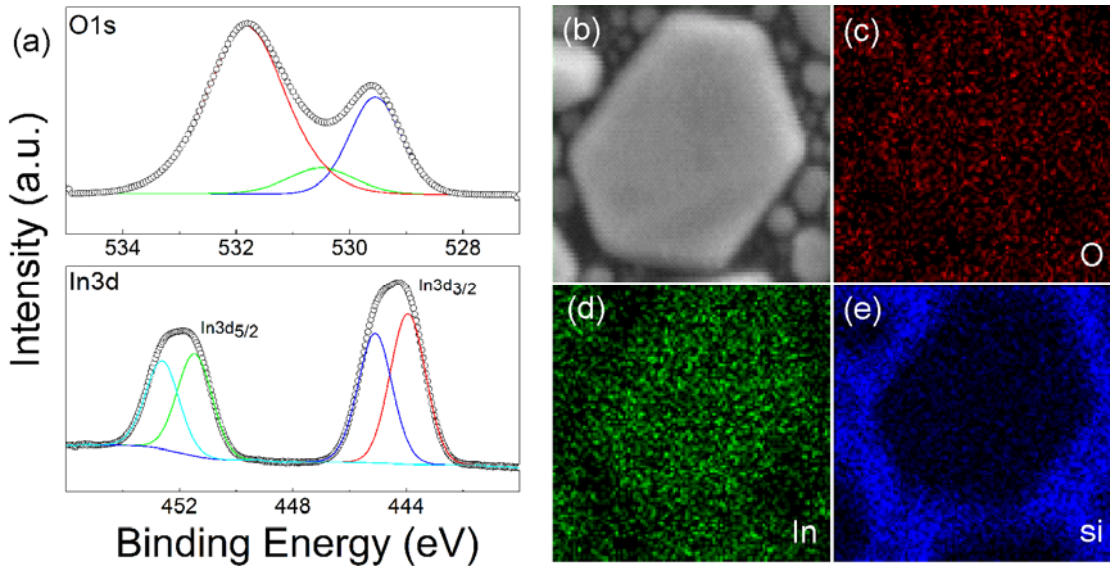

Figure 3. X-ray core-level photoelectron spectra of (a) O 1s and In 3d of the In_2O_3 nanodot dispersion. (b-e) EDX maps of In_2O_3 nanodot showing distributions of oxygen, indium and silicon respectively.

Enhanced IR transparency of In_2O_3 nanodot dispersion.

Angle resolved transmission measurements of the nanodot dispersions and an ITO thin film were determined and are summarised in Fig. 4. The position of the plasma frequency is indicated by ω_p undergoes a red shifts and the reflectance of the In_2O_3 nandots dispersion and the ITO thin film decreases with angle near their respective plasma frequencies, shown in Fig. 4a. The reflectance decreases substantially after the plasma frequency. Nanoparticle layers offer excellent visible-infrared transmission, and also antireflection properties, as seen in the optical images in Fig. 4b and c. The red-shifting of the entire angle-resolved spectrum for the nanodots dispersions is also seen in Fig. 4a, where at visible wavelengths the transmission varies from 55% at near incidence and at 40°, and importantly, remains 87% transparent at wavelengths up to 4 μm (Fig. 4a) (20).

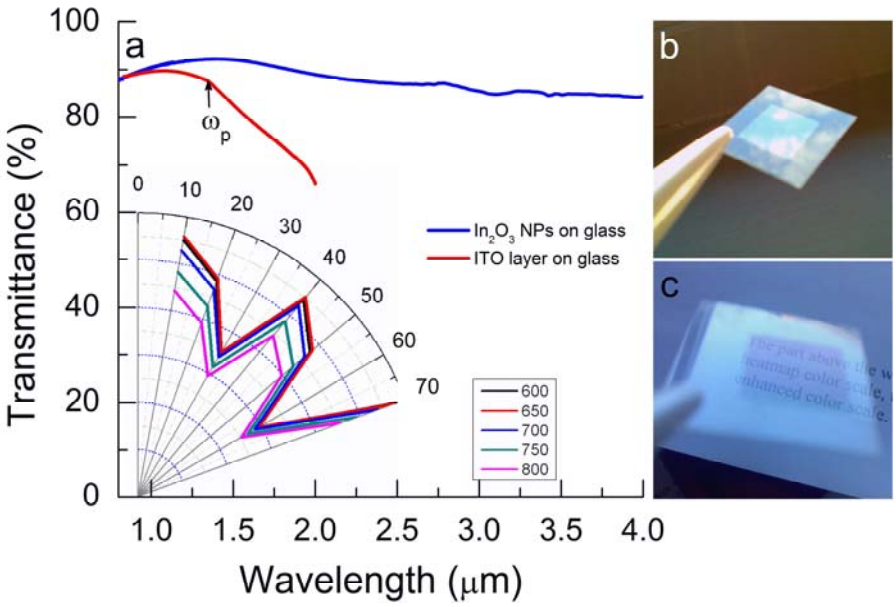

Figure 4. (a) Transmittance of the In_2O_3 nanodot dispersions and that of an ITO thin film of similar nominal thickness. (*Inset*) Polar plot of the angle-resolved transmission of the nanodots at visible wavelengths. (b,c) Optical images of the In_2O_3 nanodots showing antireflection characteristics in the visible range.

Reversible electrochemical Li-insertion

The ability of the In_2O_3 nanodot dispersions to reversibly intercalate or alloy Li, and its insertion and removal potentials, were examined using cyclic voltammetry. Figure 5a shows the cyclic voltammetric response of the Li|Li^+-electrolyte|In_2O_3(111)|Si(100) system. For this cell the cathodic process included the insertion of Li into In_2O_3 to form a Li-In alloy (charging) and the anodic process follows Li extraction or dealloying (discharging). A related process is known to occur for Li alloying with Sn (21), but there are limited investigations of Li insertion in to In-containing materials (22). During the first negative scan, two weak irreversible peaks appear at 1.2 V and 0.8 V from the reduction of In_2O_3 to In^0. Once reduced from In_2O_3 to In^0, the indium is never oxidized again in the potential range examined. Zhou *et al* . (23) have shown reoxidation after cycling the anode to upper potentials greater than 3.5 V, a voltage window typical of cathode materials. We cycled the anode in 0 - 2.5 V, a potential window below oxidation potential of In^0 (2.7 V vs. Li^+/Li) (24).

A large reversible peak appears at 0.4 V from the alloying process of Li insertion into In^0. The extent of this reaction, indicated by measured current is found to reduce with increasing cycle number. The reversible Li insertion-removal process occurs in a voltage window of 0.4 – 0.7 V are the reversible processes described by $zLi^+ + ze^- + In \leftrightarrow Li_zIn \quad (0 < z \leq 4.33)$. For Li|$Li^+$-electrolyte|$In_2O_3$(111)|Si(100), buffering of polarization effects is provided by the Si current collector, which can accommodate the highest Li storage capacity of all anode materials (25,26).

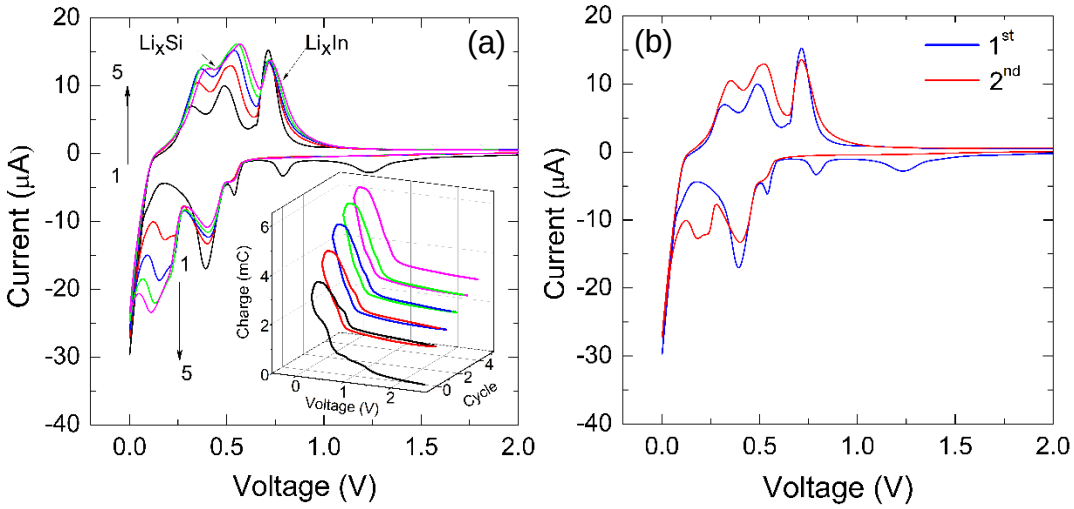

Figure 5. (a) Cyclic voltammetry of In_2O_3 nanodot electrodes between 0.0 – 2.5 V. Inset shows the corresponding integrated charge vs. voltage curve for 5 cycles. (b) Cyclic voltammograms for first and second cycle highlighting the SEI layer formation.

The free surface area (~20%) between neighbouring particles allows Li to be co-inserted into the silicon current collector, which is indicated by the existence of two additional peaks in the anodic part of the insertion reaction, at 0.32 V and 0.5 V. Those peaks relate to the removal of lithium from silicon (25). Figure 5b shows the first 2 cycles of this system, and we note that the reduction of In_2O_3 and related alloying processes dominate over Li_xSi phase formation and insertion of lithium into silicon in the first cycle. This co-insertion into the active material and current collector equilibrates after the second cycle. The increasing rate of Li-Si formation can be attributed to an activation effect (26) linked to lithiation-induced volumetric expansion that causes cracking and the exposure of unreacted material to the electrolyte. Successive cycling then allows more lithium to intercalate into silicon, providing a degree of stress buffering for the In alloying process without requiring carbon, conductive additives or polymeric binders. The rate of alloying and dealloying, insertion and removal are consistently balanced in each cycle (Fig. 5a, inset), and apart from charge associated with SEI formation and reduction to In^0, negligible charge fading is found for *all* processes in all subsequent cycles.

During co-insertion into the active material and current collector, both of which are reversible, the variation in volumetric changes and accompanying effects is considered. The SEM images in Figs 6a and b show the condition of the electrode surface before and after cycling. The brightness of the secondary electron emission stems from a reduced conductivity of the Li_xIn phase. As the nanodots are epitaxial, their adhesion to the substrate is excellent, and lithium insertion is not likely to occur directly under each nanodot, unless they are extremely small. In this case, we note that some of the smallest nanodots are removed from the substrate, but this occurs when their diameter is less than the change in volume of the near surface of the silicon. The molar volume of In^0 is a factor of 2.45 less than the In_2O_3 and by comparison to the size reduction observed, it is clear that no significant volume change effects occur in stable In^0 nanodots faceting related to the structure of In_2O_3 is also lost during electrochemical reduction to the pure metal.

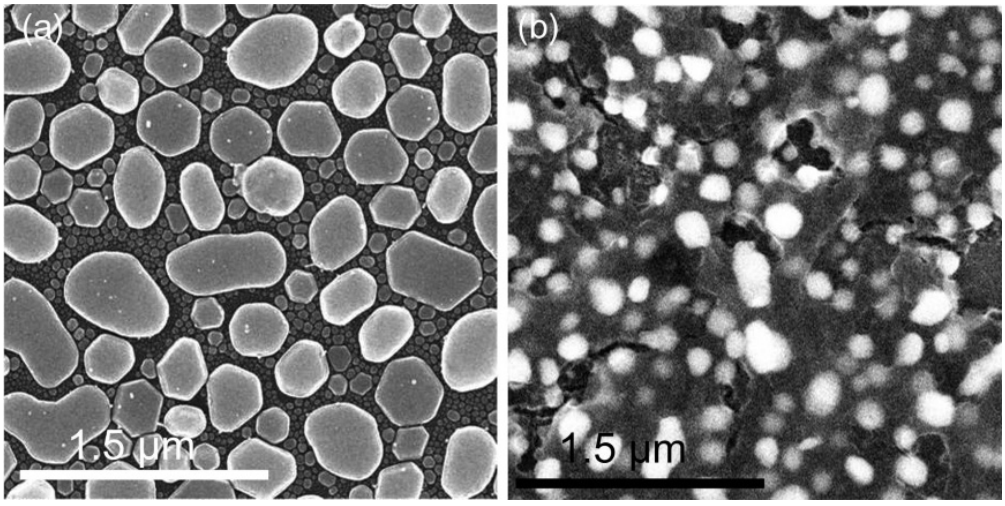

Figure 6. SEM images showing nanodots (a) and (b) after electrochemical cycling.

Conclusions

The unique size dispersion of In_2O_3 nanodots prepared by MBE deposition of indium and subsequent oxidation in air at elevated temperature, has allowed the development of a Li-ion battery electrode with enhanced IR transparency without sacrificing electrical conductivity, and lithium co-insertion processes with high Coulombic efficiency that results in stable cycling and charge storage. The In_2O_3 nanodots show bimodal size distribution confirming a two-step epitaxial growth mechanism, and good surface coverage with unique shape and (111) crystalline orientation. The nanodot dispersions were successfully shown to reversibly alloy with lithium after reduction to metallic indium; the specific size distributions allow reversible lithium co-insertion with a silicon current collector as well as the active material on the surface. Moreover, the specific size offers excellent antireflective properties and enhanced transparency reaching ~87% at 4 µm, potentially allowing for further development of transparent battery electrodes or the possibility for *in-situ* non-destructive spectroscopic monitoring of structural and electrochemical processes.

Acknowledgements

MO and EA acknowledge the support of the Irish Research Council under awards RS/2010/2170 and RS/2010/2920. WK and CMST acknowledge support from the Spanish MINECO projects ACPHIN (FIS2009-10150) and TAPHOR (MAT2012-31392), the CONSOLIDER project nanoTHERM (CSD2010-00044) and the Catalan AGAUR grant 2009-SGR-150. COD acknowledges support from Science Foundation Ireland under award no. 07/SK/B1232a and from UCC Strategic Research Fund. The authors thank F. Laffir and C. Dickinson for assistance in XPS and EBSD measurements.

References

1. D. S. Ginley and C. Bright, *MRS Bull.*, **25**, 15–18 (2011).
2. C. H. Chiu, P. Yu, C. H. Chang, C. S. Yang, M. H. Hsu, H. C. Kuo, and M. a Tsai, *Opt. Express.*, **17**, 21250–6 (2009).
3. P.-C. Chen et al., *ACS nano*, **3**, 3383–90 (2009).

4. N. R. Armstrong, P. A. Veneman, E. Ratcliff, D. Placencia, and M. Brumbach, *Acc.Chem. Res.*, **42**, 1748–57 (2009).
5. C. O'Dwyer, M. Szachowicz, G. Visimberga, V. Lavayen, S. B. Newcomb, and C. M. S. Torres, *Nat. Nanotechnol.*, **4**, 239–44 (2009).
6. H. K. Yu, W. J. Dong, G. H. Jung, and J.-L. Lee, *ACS nano*, **5**, 8026–32 (2011).
7. P.-C. Hsu, H. Wu, T. J. Carney, M. T. McDowell, Y. Yang, E. C. Garnett, M. Li, L. Hu, and Y. Cui, *ACS nano*, **6**, 5150–6 (2012).
8. K. S. Kim et al., *Nature*, **457**, 706–10 (2009).
9. J.-Y. Lee, S. T. Connor, Y. Cui, and P. Peumans, *Nano Lett.*, **8**, 689–92 (2008).
10. D. Lin, H. Wu, R. Zhang, and W. Pan, *Nanotechnology*, **18**, 465301 (2007).
11. S. Kim, S. Ju, J. H. Back, Y. Xuan, P. D. Ye, M. Shim, D. B. Janes, and S. Mohammadi, *Adv. Mater.*, **21**, 564–568 (2009).
12. K. Samedov, Y. Aksu, and M. Driess, *Chem. Mater.*, **24**, 2078–2090 (2012).
13. Y. Yang, S. Jeong, L. Hu, H. Wu, S. W. Lee, and Y. Cui, *P. Natl. Acad. Sci.*, **108**, 13013–8 (2011).
14. Z. Wu et al., *Science*, **305**, 1273–6 (2004).
15. T. M. Barnes, X. Wu, J. Zhou, a. Duda, J. van de Lagemaat, T. J. Coutts, C. L. Weeks, D. a. Britz, and P. Glatkowski, *Appl. Phys. Lett.*, **90**, 243503 (2007).
16. M. Zhang, S. Fang, A. a Zakhidov, S. B. Lee, A. E. Aliev, C. D. Williams, K. R. Atkinson, and R. H. Baughman, *Science*, **309**, 1215–9 (2005).
17. H.-K. Kim, D.-G. Kim, K.-S. Lee, M.-S. Huh, S. H. Jeong, K. I. Kim, and T.-Y. Seong, *Appl. Phys. Lett.*, **86**, 183503 (2005).
18. P. D. C. King and T. D. Veal, *J. Phys.: Condens. Matter*, **23**, 334214 (2011).
19. C. a Schneider, W. S. Rasband, and K. W. Eliceiri, *Nat. Methods*, **9**, 671–675 (2012).
20. D. M. Follstaedt, *Appl. Phys. Lett.*, **62**, 1116 (1993).
21. J. S. Chen and X. W. (David) Lou, *Mater. Today*, **15**, 246–254 (2012).
22. H. Geaney, T. Kennedy, C. Dickinson, E. Mullane, A. Singh, F. Laffir, and K. M. Ryan, *Chem. Mater.*, **24**, 2204–2210 (2012).
23. Y. Zhou, H. Zhang, M. Xue, C. Wu, X. Wu, and Z. Fu, *J. Power Sources*, **162**, 1373–1378 (2006).
24. J. Vanhees, J. P. Francois, and L. C. Van Poucke, *J. Phys. Chem.*, **85**, 1713–1718 (1981).
25. C. K. Chan, H. Peng, G. Liu, K. McIlwrath, X. F. Zhang, R. a Huggins, and Y. Cui, *Nat. Nanotechnol.*, **3**, 31–5 (2008).
26. C. K. Chan, R. N. Patel, M. J. O'Connell, B. a Korgel, and Y. Cui, *ACS nano*, **4**, 1443–50 (2010).
27. B.-S. Lee, S.-B. Son, K.-M. Park, J.-H. Seo, S.-H. Lee, I.-S. Choi, K.-H. Oh, and W.-R. Yu, *J. Power Sources*, **206**, 267–273 (2012).